Supporting Information

Ekman et al. 10.1073/pnas.1207523109

SI Materials and Methods

Multivariate Functional Magnetic Resonance Imaging (fMRI) Analysis. ***Defining network nodes.*** Preparation [cue: color (C) or motion (M)] and no-preparation conditions [cue: no preparation (N)] were modeled using a general linear model (GLM). Parameter estimates were registered to the MNI152 standard brain template in 2-mm resolution and subjected to an across-participant multivariate pattern analysis, using the PyMVPA software package (1). No spatial smoothing was applied. To search in an unbiased fashion for voxels that discriminate between preparation and no-preparation conditions, we used a searchlight analysis (2, 3), which examines information in local spatial patterns of brain activity surrounding each voxel. Around each gray matter voxel v_i we first defined a spherical cluster (radius = 8 mm) and extracted the parameter estimates for preparation and nonpreparation. This yielded two pattern vectors that were used to train a pattern classification algorithm. To assess the classification performance, we trained a sparse logistic regression classifier on the pattern vectors of all but one subject (default $\lambda = 0.1$). The pattern vectors of the remaining subject were used as an independent test set. This leave-one-subject-out cross-validation procedure was repeated until each subject had been used in the test set once. The resulting classification accuracy (across subjects) was assigned to the respective voxel v_i. This procedure was repeated for each voxel and resulted in a 3D accuracy map, restricted to gray matter.

To estimate the significance of classification accuracy for each voxel v_i, we conducted a nonparametric permutation test (4). To this end, the searchlight analysis was repeated 10,000 times with permuted labels. The P value for every voxel v_i was then calculated as the fraction of permutation samples that were greater than or equal to the accuracy actually observed when using correct labels. The resulting P-map (i.e., Fig. 1*B*) was corrected for multiple comparison with false discovery rate (FDR) ($q = 0.05$) and thresholded accordingly.

Brain areas involved in task preparation were used to define network nodes (5–7) for subsequent analyses. To derive nonoverlapping and equally sized network nodes, we used an iterative approach. We started by defining a sphere (radius = 12 mm) around the voxel with the lowest P value, as identified by the searchlight analysis. This sphere became the first node in the network. Then we moved to the second-lowest P value and defined the next sphere. A sphere was created only when it did not overlap with previously generated spheres. In the case of an overlap, this voxel was ignored and we selected the voxel with the next lowest P value. This procedure was repeated until no additional spheres could be created and resulted in 70 nodes. The Montreal Neurological Institute (MNI) coordinates of the spherical center coordinates are displayed in Table S1.

Graph Construction and Control Analyses. Our approach to concatenate relevant segments of the raw data time series was previously successfully applied (8–10), but might induce artifacts that need to be examined. Here we report a series of control analyses that aim to support the validity of our approach. First, we ruled out the possibility of slow mean shifts (e.g., related to changes in scanner signal) driving the correlation estimates, rather than task-related changes. To this end, we compared the average blood oxygen level dependent (BOLD) signal between all 12 subsequent task blocks, using an ANOVA across subjects. No significant differences were found [$F(11, 96) = 0.31$, $P = 0.98$]. Furthermore, to directly test the similarity of individual time courses throughout the experiment, we calculated the connectivity matrices (aggregated over all conditions) separately for each task block. Resulting connectivity matrices were tested for reliability, using the intraclass correlation coefficient (ICC) for each subject. The test showed very high consistency in the connectivity matrices across task blocks and the ICC varied across subjects between 0.89 and 0.98 [$F(2{,}414, 26{,}554) \sim 9.14$–$51.65$; all $P < 0.001$].

Second, the concatenation of the relevant time-series segments might cause spikes in the newly generated time series that could cause spurious correlations. To investigate this effect we compared the absolute difference of two volumes made adjacent by concatenation with the absolute signal difference at two naturally adjacent volumes. To this end we performed a nonparametric permutation analysis. For each subject, the averaged difference for the concatenated volumes was compared with 10,000 randomly chosen nonconcatenation differences. The P value was calculated as the amount of occurrences a difference at a nonconcatenation gave an equal or higher value than a difference at a concatenated point. For all subjects, this resulted in P values with $P > 0.3$, indicating that the concatenation does not induce more spikes in the signal than expected from a chance distribution.

Third, due to the average error rate of ∼20%, concatenated time series of incorrect trials consisted of fewer time points than those of correct trials. This might potentially influence the correlation estimates and lead to, e.g., lower correlations in the incorrect conditions. To test this effect, we compared the mean connectivity as the average over all entries of the adjacency matrix between all conditions (i.e., color/motion, correct/incorrect), using an ANOVA. No significant differences in mean connectivity were found [$F(3, 32) = 0.56$, $P = 0.65$].

Fourth, we find converging evidence for our results, using a slightly different analysis approach (β-series correlation). A commonly used alternative to our time-series concatenation approach is to model each trial of interest with a separate predictor in a GLM and concatenate the resulting β-coefficients to a so-called β-series (11–13). The correlation analysis is then applied on the β-series. Applying the same inverse modeling approach as for the concatenation approach, we could classify color vs. motion preparation with an accuracy of 84.2% motion correct vs. incorrect with 72.2% accuracy and color correct vs. incorrect with 61.1% accuracy. Note, however, whereas this can be seen as converging evidence for our results, it might not be regarded as a fair comparison of both analysis approaches. The β-time series is substantially shorter (only one β per trial) and differences in the classification accuracy might be due to higher power in the raw time-series approach.

Stability of the Core Across Task Conditions. One of our main findings is the enhanced closeness of task-relevant visual areas to the network core. However, because the k-core decomposition was applied to the averaged connectivity matrices across all conditions, it is important to show that changes in core closeness cannot be attributed to changes in the core structure itself. To this end, we performed the k-core decomposition with all conditions separately. As the results show, the core remains highly stable across conditions (Fig. S3). This is in line with the observation that incorrect trials are not characterized by a global reduction in connectivity, but rather by specific core–periphery interactions.

Graph Theory Formulas. Network measures were calculated with networkX (http://networkx.lanl.gov), and a detailed description of all formulas can be found elsewhere (7). N is the set of all nodes in the network and n is the number of nodes. w_{ij} is the connection weight between i and j $(i,j \in N)$.

Local weighted degree. The weighted degree of a node i is the sum of all edge weights connected to that node:

$$k_i = \sum_{j \in N} w_{ij}.$$

Global degree.

$$k = \frac{1}{n} \sum_{i \in N} k_i.$$

Average shortest path length.

$$L = \frac{1}{n} \sum_{i \in N} L_i = \frac{1}{n} \sum_{i \in N} \frac{\sum_{j \in N \ \ j \neq i} d_{ij}}{n-1},$$

where d_{ij} is the shortest path length between nodes i and j. For the path length calculation of weighted networks the connection weights w_{ij} were transformed to distances, using the inverse transform $wd_{ij} = 1/w_{ij}$.

Local clustering coefficient. The clustering of each node i is the fraction of possible triangles that exist around i,

$$C_i = \frac{2t_i}{k_i\,(k_i - 1)},$$

where t_i is the number of triangles around node i, and

$$t_i = \frac{1}{2} \sum_{j,h \epsilon N} \left(w_{ij} w_{ih} w_{jh} \right)^{1/3}.$$

Global clustering coefficient.

$$C_{\text{glob}} = \frac{1}{n} \sum_{i \in N} C_i,$$

where C_i is the local clustering coefficient.

Assortativity.

$$r = \frac{l^{-1} \sum_{(i,j) \in L} w_{ij} k_i k_j - \left[l^{-1} \sum_{(i,j) \in L} \frac{1}{2} w_{ij} \left(k_i + k_j \right) \right]^2}{l^{-1} \sum_{(i,j) \in L} \frac{1}{2} w_{ij} \left(k_i^2 + k_j^2 \right) - \left[l^{-1} \sum_{(i,j) \in L} \frac{1}{2} w_{ij} \left(k_i + k_j \right) \right]^2}.$$

Transitivity.

$$T = \frac{\sum_{i \in N} 2t_i}{\sum_{i \in N} k_i (k_i - 1)}.$$

Modularity. Modularity was calculated using an iterative algorithm (14). The results were averaged over 100 repetitions,

$$Q = \frac{1}{l^w} \sum_{i,j \in N} \left[w_{ij} - \frac{k_i^W k_j^W}{l^W} \right] \delta_{m_i m_j},$$

where m_i is the module containing node i, and $\delta_{m_i m_j} = 1$ if $m_i = m_j$ and 0 otherwise. The concept of finding modules by modularity optimization is fundamentally different from the concept of k-shell decomposition. Optimizing the modularity function will yield a network structure of densely connected nodes within a module and sparse connections between modules. In contrast, k-shell decomposition will find a densely connected "core" that is well connected to the periphery, but the periphery is mostly sparsely interconnected with many connections crossing the core.

Efficiency global.

$$E_{\text{glob}} = \frac{1}{n(n-1)} \sum_{i \neq j \in N} \frac{1}{d_{ij}}.$$

Efficiency cost.

$$E_{\text{cost}} = E_{\text{glob}} - K,$$

where the wiring costs K are determined as the sum of edge weights between the connected nodes, divided by the maximum possible value of edge weights (15).

Efficiency local.

$$E_{\text{local}} = \frac{1}{n_{Gi}(n_{Gi} - 1)} \sum_{j,k \in G_i} \frac{1}{d_{j,k}},$$

where n_{Gi} is the number of nodes in the subgraph G_i.

Efficiency nodal.

$$E_{\text{nodal}}(i) = \frac{1}{(n-1)} \sum_{j \in G} \frac{1}{d_{ij}}.$$

Small-world scalar.

$$S = \frac{C/C_{\text{rand}}}{l/l_{\text{rand}}}.$$

C and l are coefficients of the tested network (clustering and average shortest path length) and C_{rand} and l_{rand} are the respective values of a randomized version of the original network with the same degree distribution (16, 17). C_{rand} and l_{rand} were obtained by calculating the average values of 100 randomizations.

Betweenness centrality.

$$\text{BC}_i = \frac{1}{(n-1)(n-2)} \sum_{s,t \in N} \frac{n_{st}^i}{g_{st}},$$

where $n^i{}_{st}$ is the number of shortest paths from s to t that pass through i and g_{st} is the total number of shortest paths from s to t.

Current flow betweenness centrality. In contrast to betweenness centrality, which uses shortest paths, current-flow betweenness centrality (18), also known as random-walk betweenness centrality (19), uses an electrical current model for information spreading. Given a supply b, the throughput of a node $i \in N$ is defined to be

$$\tau(i) = \frac{1}{2} \left(-|b(i)| + \sum_{e: i \in e} |x(e^{\rightarrow})| \right).$$

Current flow betweenness centrality is defined by

$$\text{CFBC}_i = \frac{1}{(n-1)(n-2)} \sum_{s,t \in N} \tau_{st}(i).$$

Eigenvector centrality. Eigenvector centrality is an extension of the degree centrality measure. Instead of counting the amount of neighbors, the eigenvector centrality of a node is defined proportionally to the sum of importance of its neighbors (20). We used the eigenvector centrality implementation of Networkx (21), which uses the power method to find the eigenvector for the largest eigenvalue of the adjacency matrix.

Closeness centrality. Closeness centrality (20) is a centrality measure that reflects the inverse average distance to all nodes in the network,

$$\mathrm{CLC}_i = \frac{1}{l_i},$$

where

$$l_i = \frac{\sum_{j(\neq i)\in N} d_{ij}}{n-1}.$$

PageRank. The PageRank algorithm (22) is an iterative procedure that was developed in the context of web searching to find how often a node will be visited during random network traversal,

$$\mathrm{PR}_i = \frac{1-\lambda}{N} + \lambda \sum_{n_j\in M(n_i)} \frac{\mathrm{PR}(n_j)}{O(n_j)},$$

where $M(n_i)$ is the set of nodes that link to n_i, $\mathrm{PR}(n_j)$ denotes the PageRank of node v_j, and $O(n_j)$ is the out degree of the predecessor node n_j. The PageRank algorithm was originally designed for directed graphs. Here we apply it to undirected graphs with default $\lambda = 0.85$, where the out degree equals in degree equals degree.

Vulnerability. The vulnerability (23) is a measure of centrality. Vulnerability at a node n_i is the relative change in the sum of distances between all node pairs when excluding that node,

$$V_i = \frac{L_G - L_H}{L_G},$$

where L_G is the sum of distances between all nodes including n_i and L_H is the sum of distances between all nodes without n_i.

Core closeness. Core closeness is an extension of closeness centrality informed by the network's core–periphery structure. Closeness centrality is calculated for a node in the periphery P with respect to the core C.

The core closeness of a node $i \in P$ and $i \notin C$ is given by

$$\mathrm{CCL}_{i\in P} = \frac{1}{l_i},$$

where

$$l_i = \sum_{j\in C} d_{ij}.$$

Core centrality. Core centrality is an extension of betweenness centrality informed by the network's core–periphery structure. It reflects the number of shortest paths with start and end points in the periphery that pass through the core. The concept of core centrality is analogous to the previously introduced rich-club centrality (24),

$$\mathrm{CC} = \sum_{s,t\in P} \frac{n_{st}^C}{g_{st}^P},$$

where C and P are distinct subgraphs of the graph G. $n^C{}_{st}$ is the number of shortest paths from s to $t \in P$ that pass through C and g_{st}^P is the total number of shortest paths from s to $t \in P$.

Correlation of Graph Theory Metrics. In this study we use a large selection of different graph metrics of which several are based on similar concepts (e.g., centrality) and therefore might be highly correlated. To explore these relationships we calculated the Pearson cross-correlation of the used local graph metrics separately for all conditions (Fig. S1*A*). The resulting correlation coefficients varied between −0.3 and 0.7. As shown before (25), the intercorrelation of the graph metrics differed between experimental conditions, which confirms previous findings (26) that, depending on the network topology, these graph metrics differ in their ability to extract complex network characteristics. However, a subset of graph metrics appeared to be highly correlated, namely degree, efficiency nodal, eigenvector centrality, closeness centrality, and PageRank. Also, betweenness centrality and current flow betweenness centrality showed a moderate correlation.

To further explore whether the intercorrelation had an effect on the classification analysis, we tested the ability of different graph metrics to distinguish between color and motion preparation. To this aim, we applied the classification analysis to individual local graph metrics. As the results showed (Fig. S1*B*), none of the highly correlated metrics was able to distinguish between color and motion preparation. Importantly, all metrics that contributed to the prediction of the combined model also resulted in significant classification accuracies when regarded in isolation (including betweenness centrality and current flow betweenness centrality). The results also show that the integration into one statistical model leads to a further increase in classification performance, highlighting the advantage of our inverse network modeling approach.

Although our study employs a large set of graph theoretical metrics, no measures were used that quantify the efficiency of physical embedding of complex networks (27, 28). Future studies might therefore also consider using these measures to investigate network changes. Also, most of the graph metrics used are based on the concept of shortest paths, whereas recent studies introduced metrics to investigate information flow using random walks between any two nodes and emphasize the role of non-shortest paths for brain communication (29–31). These metrics have been shown to reveal changes in brain structure after stroke (32) and might be worth applying to fMRI in future studies.

Influence of Head Movement. It has been shown that head movement can have an impact on functional connectivity estimates (33). In our investigation it is especially important to ensure that there are no condition-specific head movements that might act as a confound for the classification analysis. To this end, we compared the root-mean-square (rms) of the estimated translation parameters (33) across conditions. An ANOVA found no significant differences [$F(3, 32) = 0.07$; $P = 0.97$]. Also a more detailed analysis of the frequencies of different displacements revealed no differences between conditions (Fig. S2).

1. Hanke M, et al. (2009) PyMVPA: A python toolbox for multivariate pattern analysis of fMRI data. *Neuroinformatics* 7:37–53.
2. Clithero JA, Smith DV, Carter RM, Huettel SA (2011) Within- and cross-participant classifiers reveal different neural coding of information. *Neuroimage* 56:699–708.
3. Kriegeskorte N, Goebel R, Bandettini P (2006) Information-based functional brain mapping. *Proc Natl Acad Sci USA* 103:3863–3868.
4. Nichols TE, Holmes AP (2002) Nonparametric permutation tests for functional neuroimaging: A primer with examples. *Hum Brain Mapp* 15:1–25.
5. Rubinov M, Sporns O (2010) Complex network measures of brain connectivity: Uses and interpretations. *Neuroimage* 52:1059–1069.
6. Bullmore E, Sporns O (2009) Complex brain networks: Graph theoretical analysis of structural and functional systems. *Nat Rev Neurosci* 10:186–198.
7. Rubinov M, Sporns O (2010) Complex network measures of brain connectivity: Uses and interpretations. *Neuroimage* 52:1059–1069.
8. Kayser AS, Sun FT, D'Esposito M (2009) A comparison of Granger causality and coherency in fMRI-based analysis of the motor system. *Hum Brain Mapp* 30:3475–3494.

9. Lauritzen TZ, D'Esposito M, Heeger DJ, Silver MA (2009) Top-down flow of visual spatial attention signals from parietal to occipital cortex. *J Vis* 9:11–14.
10. Sun FT, Miller LM, D'Esposito M (2004) Measuring interregional functional connectivity using coherence and partial coherence analyses of fMRI data. *Neuroimage* 21:647–658.
11. Chadick JZ, Gazzaley A (2011) Differential coupling of visual cortex with default or frontal-parietal network based on goals. *Nat Neurosci* 14:830–832.
12. Gazzaley A, Rissman J, D'Esposito M (2004) Functional connectivity during working memory maintenance. *Cogn Affect Behav Neurosci* 4:580–599.
13. Rissman J, Gazzaley A, D'Esposito M (2004) Measuring functional connectivity during distinct stages of a cognitive task. *Neuroimage* 23:752–763.
14. Blondel VD, Guillaume J-L, Lambiotte R, Lefebvre E (2008) Fast unfolding of communities in large networks. *J Stat Mech*, 10.1088/1742-5468/2008/10/P10008.
15. Achard S, Bullmore E (2007) Efficiency and cost of economical brain functional networks. *PLoS Comput Biol* 3:e17.
16. Milo R, et al. (2002) Network motifs: Simple building blocks of complex networks. *Science* 298:824–827.
17. Sporns O, Kötter R (2004) Motifs in brain networks. *PLoS Biol* 2:e369.
18. Brandes U, Fleischer D (2005) Centrality measures based on current flow. *Proceedings of the 22nd Symposium on Theoretical Aspects of Computer Science (STACS '05)*, eds Diekert V, Durand B (Springer, Berlin), pp 533–544.
19. Newman (2005) A measure of betweenness centrality based on random walks. *Social Networks* 27:39–54.
20. Newman MEJ (2010) *Networks: An Introduction* (Oxford Univ Press, Oxford).
21. Hagberg AA, Schult DA, Swart PJ (2008) Exploring network structure, dynamics, and function using NetworkX. *Proceedings of the 7th Python in Science Conference (SciPy2008)*, eds Varoquaux G, Vaught T, Miillman J, pp 11–15. Available at http://conference.scipy.org/proceedings/SciPy2008/index.html.
22. Brin S, Page L (1998) The anatomy of a large-scale hypertextual web search engine. *Seventh International World-Wide Web Conference (WWW 1998)* (Brisbane, Australia). Available at http://ilpubs.stanford.edu:8090/361/.
23. Costa LDF, Rodrigues FA, Travieso G, Villas Boas PR (2007) Characterization of complex networks: A survey of measurements. *Adv Phys* 56:167–242.
24. van den Heuvel MP, Sporns O (2011) Rich-club organization of the human connectome. *J Neurosci* 31:15775–15786.
25. Bassett DS, Meyer-Lindenberg A, Achard S, Duke T, Bullmore E (2006) Adaptive reconfiguration of fractal small-world human brain functional networks. *Proc Natl Acad Sci USA* 103:19518–19523.
26. Zuo XN, et al. (2012) Network centrality in the human functional connectome. *Cereb Cortex* 22:1862–1875.
27. Bassett DS, et al. (2010) Efficient physical embedding of topologically complex information processing networks in brains and computer circuits. *PLoS Comput Biol* 6: e1000748.
28. Bullmore E, Sporns O (2012) The economy of brain network organization. *Nat Rev Neurosci* 13:336–349.
29. da Fontoura Costa L, Batista JL, Ascoli GA (2011) Communication structure of cortical networks. *Front Comput Neurosci*, 10.3389/fncom.2011.00006.
30. Estrada E, Hatano N (2008) Communicability in complex networks. *Phys Rev E Stat Nonlin Soft Matter Phys* 77:036111.
31. Rodrigues FA, da Fontoura Costa L (2009) A structure-dynamic approach to cortical organization: Number of paths and accessibility. *J Neurosci Methods* 183:57–62.
32. Crofts JJ, et al. (2011) Network analysis detects changes in the contralesional hemisphere following stroke. *Neuroimage* 54:161–169.
33. Van Dijk KR, Sabuncu MR, Buckner RL (2012) The influence of head motion on intrinsic functional connectivity MRI. *Neuroimage* 59:431–438.

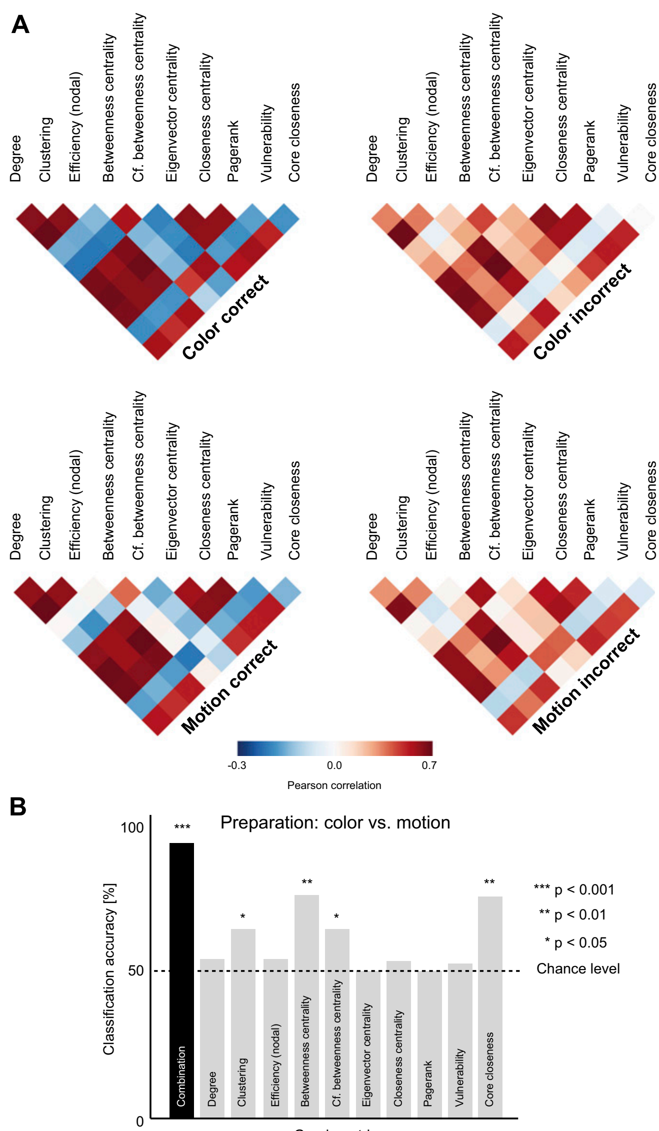

Fig. S1. (*A*) Correlation of local graph metrics. (*B*) Classification accuracy for all local graph metrics separately and combined in one statistical model.

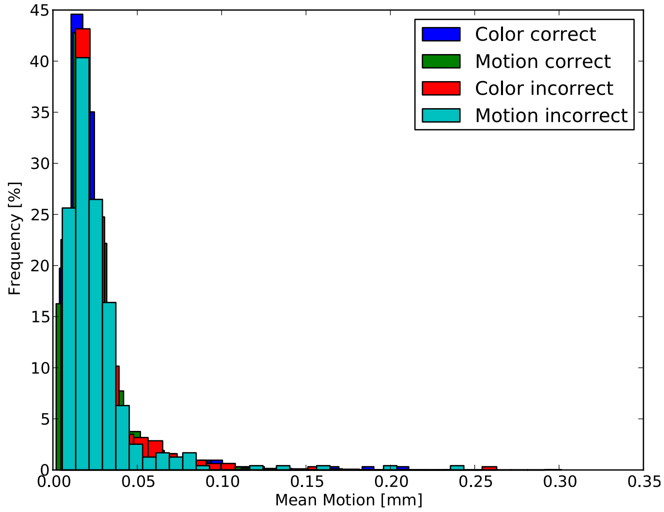

Fig. S2. Frequency distribution of condition-specific mean head motion, averaged across all subjects.

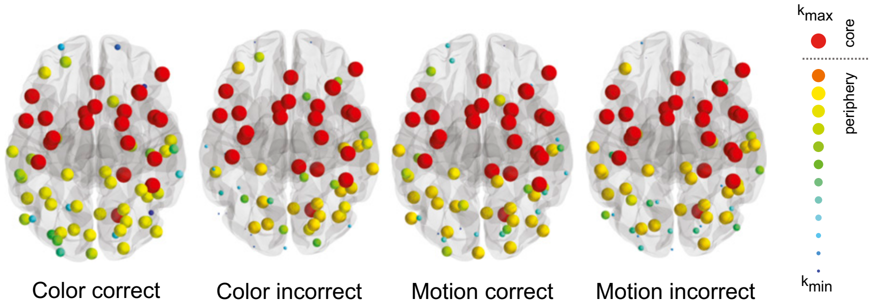

Fig. S3. Stable core across different task conditions. Shown are the results of the *k*-shell scores for every node, separately for color correct/incorrect and for motion correct/incorrect. Nodes with the maximal *k*-shell value (red) form the core and all other regions <*k*(max) are the periphery.

Table S1. Center coordinates and core/periphery allocation of all 70 network nodes

Node	Anatomical region	Lat.	Coordinates *x*	*y*	*z*	Module
1	Inferior frontal junction	L	−53	3	39	Core
2	Inferior frontal gyrus	L	−48	22	14	Core
3	Postcentral sulcus	L	−43	−28	35	Core
4	Inferior precentral sulcus	L	−38	5	24	Core
5	Posterior insula	L	−34	−13	8	Core
6	Superior precentral sulcus	L	−32	−10	52	Core
7	Caudate nucleus	L	−7	9	4	Core
8	Medial superior frontal gyrus	L	−6	2	66	Core
9	Medial SFG/cingulate gyrus	B	0	14	44	Core
10	Cingulate gyrus	B	2	33	19	Core
11	Posterior cingulate gyrus	R	8	−36	42	Core
12	Cerebellum	R	18	−69	−31	Core
13	Superior frontal gyrus	R	21	1	70	Core
14	Parahippocampal gyrus	R	22	−38	−14	Core
15	Superior frontal sulcus	R	23	10	51	Core
16	Superior precentral sulcus	R	25	−14	57	Core
17	Deep FO/anterior insula	R	34	25	3	Core
18	Middle frontal gyrus	R	34	24	34	Core
19	Postcentral sulcus	R	43	−22	41	Core
20	Angular gyrus	R	44	−46	36	Core
21	Frontal operculum	R	46	6	6	Core
22	Postcentral gyrus	R	46	−26	62	Core
23	Inferior frontal junction	R	50	4	36	Core
24	Inferior frontal gyrus	R	52	39	2	Core
25	Postcentral sulcus	L	−63	−20	29	Periphery
26	Supramarginal gyrus	L	−57	−38	45	Periphery
27	Superior temporal gyrus	L	−56	−40	14	Periphery
28	Anterior occipital sulcus (~hMT)	L	−53	−72	−6	Periphery
29	Inferior temporal gyrus	L	−52	−56	−22	Periphery
30	Lateral occipital cortex	L	−48	−72	16	Periphery
31	Lateral occipitotemporal sulcus	L	−48	−26	−19	Periphery
32	Intraparietal sulcus	L	−38	−52	42	Periphery
33	Inferior frontal gyrus	L	−38	40	0	Periphery
34	Fusiform gyrus	L	−34	−61	−5	Periphery
35	Cerebellum	L	−33	−84	−30	Periphery
36	Hippocampus/parahippocampal gyrus	L	−30	−10	−22	Periphery
37	Intraparietal sulcus	L	−29	−88	32	Periphery
38	Occipital pole	L	−26	−97	−5	Periphery
39	Lateral occipital cortex	L	−26	−83	13	Periphery
40	Intermediate frontal sulcus	L	−26	60	6	Periphery
41	Middle frontal gyrus	L	−22	48	28	Periphery
42	Postcentral gyrus	L	−21	−38	72	Periphery
43	Parieto-occipital fissure	L	−20	−63	28	Periphery
44	Fusiform gyrus (~V4)	L	−16	−80	−14	Periphery
45	Superior parietal lobule	L	−14	−62	52	Periphery
46	Parieto-occipital fissure	B	−4	−84	43	Periphery
47	Occipital pole	B	−2	−98	0	Periphery
48	Cuneus	B	4	−68	6	Periphery
49	Cingulate sulcus, marginal ramus	R	12	−44	68	Periphery
50	Orbitofrontal cortex	R	14	18	−18	Periphery
51	Transverse occipital sulcus	R	16	−84	26	Periphery
52	Frontomarginal gyrus	R	17	60	−15	Periphery
53	Parieto-occipital fissure	R	19	−81	49	Periphery
54	Intraparietal sulcus	R	22	−64	38	Periphery
55	Occipital pole	R	22	−94	4	Periphery
56	Collateral sulcus (~V4)	R	24	−74	−6	Periphery
57	Parahippocampal gyrus	R	28	−16	−24	Periphery
58	Superior parietal lobule	R	35	−50	59	Periphery
59	Orbitofrontal cortex	R	38	29	−19	Periphery
60	Lateral occipital cortex	R	38	−74	18	Periphery
61	Fusiform gyrus	R	40	−54	−9	Periphery

Table S1. Cont.

Node	Anatomical region	Lat.	Coordinates x	y	z	Module
62	Cerebellum	R	40	−74	−24	Periphery
63	Intraparietal sulcus	R	43	−67	43	Periphery
64	Lateral occipital cortex (~hMT)	R	47	−82	−2	Periphery
65	Cerebellum	R	47	−49	−30	Periphery
66	Angular gyrus	R	48	−52	14	Periphery
67	Parietal operculum	R	54	−20	18	Periphery
68	Superior temporal sulcus	R	58	−12	−10	Periphery
69	Postcentral gyrus	R	60	−18	44	Periphery
70	Temporoparietal junction	R	65	−38	27	Periphery

B, bilateral; FO, frontal operculum; L, left hemisphere; Lat., lateralization; R, right hemisphere; SFG, superior frontal gyrus.

Table S2. Values of discriminative local graph measures for correct and incorrect color and motion preparation within the relevant nodes

	Correct				Incorrect			
	BC	CFBC	*C*	CCL	BC	CFBC	*C*	CCL
Color								
V4 L	0.015	—	0.781	0.503	0.003	—	0.510	0.146
V4 R	0.010	—	0.729	0.476	0.006	—	0.519	0.167
hMT L	0.010	—	0.336	0.368	0.019	—	0.789	0.434
hMT R	—	0.019	0.365	0.366	—	0.029	0.767	0.415
Motion								
V4 L	0.003	—	0.410	0.201	0.026	—	0.789	0.418
V4 R	0.011	—	0.419	0.291	0.019	—	0.767	0.373
hMT L	0.013	—	0.794	0.475	0.007	—	0.326	0.220
hMT R	—	0.029	0.810	0.455	—	0.025	0.358	0.202

BC, betweenness centrality; *C*, clustering coefficient; CCL, core closeness; CFBC, current flow betweenness centrality.